scientific reports

Check for updates

OPEN

Bioconvective Reiner–Rivlin nanofluid flow over a rotating disk with Cattaneo–Christov flow heat flux and entropy generation analysis

Yu-Pei Lv[1], Hina Gul[2], Muhammad Ramzan[2✉], Jae Dong Chung[3] & Muhammad Bilal[4]

The non-Newtonian fluids possess captivating heat transfer applications in comparison to the Newtonian fluids. Here, a new type of non-Newtonian fluid named Reiner–Rivlin nanofluid flow over a rough rotating disk with Cattaneo–Christov (C–C) heat flux is studied in a permeable media. The stability of the nanoparticles is augmented by adding the gyrotactic microorganisms in the nanofluid. The concept of the envisaged model is improved by considering the influences of Arrhenius activation energy, chemical reaction, slip, and convective conditions at the boundary of the surface. The entropy generation is evaluated by employing the second law of thermodynamics. The succor of the Shooting scheme combined with the bvp4c MATLAB software is adapted for the solution of extremely nonlinear system of equations. The noteworthy impacts of the evolving parameters versus engaged fields are inspected through graphical illustrations. The outcomes show that for a strong material parameter of Reiner–Rivlin, temperature, and concentration profiles are enhanced. The behavior of Skin friction coefficients, local Nusselt number, Sherwood number, and local density number of motile microorganisms against the different estimates of emerging parameters are represented in tabular form. The authenticity of the intended model is tested by comparing the presented results in limiting form to an already published paper. A proper correlation between the two results is attained.

List of symbols

C_f	Drag force
B_2	Convection diffusion parameter
(u, v, w)	Velocity components
E_a	Activation energy coefficient
K_r	Chemical reaction rate constant
c_p	Capacity of specific heat
Sc	Schmidt number
K	Fluid parameter
D_B	Coefficient of Brownian diffusion
Sh_x	Sherwood number
T_w	Temperature on wall
Br	Brinkman number
Wc	Constant speed of cell swimming
C_∞	Concentration in the free stream
u_w	Axial route having a velocity
L	Diffusion parameter
Re	Reynolds number

[1]Department of Mathematics, Huzhou University, Huzhou 313000, People's Republic of China. [2]Department of Computer Science, Bahria University, Islamabad 44000, Pakistan. [3]Department of Mechanical Engineering, Sejong University, Seoul 143-747, Korea. [4]University of Lahore, Gujrat Campus, Gujrat 50700, Pakistan. ✉email: mramzan@bahria.edu.pk

Nu_x	Local density number
q^*	Non uniform heat source/sink
C_s	Solid surface heat capacity
Pe	Peclet number
κ	Thermal conductivity
T	Fluid temperature
N_b	Brownian motion parameter
N_G	Entropy rate
D_T	Coefficient of thermophoretic diffusion
E	Activation energy parameter
T_∞	Diffusive temperature
h_f	Convective heat transfer coefficient
h_s	Mass transfer coefficient
Pr	Prandtl number
N_t	Thermophoresis parameter
A, B	Space and temperature-dependent heat generation and absorption parameters
D_m	Microorganism's diffusivity
C	Fluid concentration
Lb	Lewis number
B_1	Biot number
Sc	Schmidt number
L, L_1	Diffusion parameters
A^*, B^*	Source, sink coefficients
Br	Brinkman number
N_∞	Ambient motile density

Greek letters

γ	Thermal relaxation time
Ω	Angular velocity
ρ	Density of fluid
$\sigma_1, \sigma_2, \sigma_3$	Temperature, concentration and motile ratio parameter
ν	Kinematic viscosity
λ	Permeability parameter
μ	Liquid dynamic viscosity
β_1, β_2	Radial and azimuthal slip parameters
α_1, α_2	Radial and azimuthal slip coefficients
λ_2	Thermal relaxation factor
δ	Ratio of the diffusion coefficient
τ_w	Shear stress (kg/ms^2)

Fluids that do not abide by the Newtonian constitutive relations like large molecular weight polymers are commonly used in lubricants, nylon, blood, clay, detergents, and paints, etc. are named as non-Newtonian fluids. The stress within the viscoelastic fluids remained alive up to some extent upon the removal of stress forces owing to the strong binding of intermolecular trussing. This inimitable feature is characterized as the memory effect. Reiner[1] and Rivlin[2] introduced a new kind of non-Newtonian fluid that adequately forecast the flow behavior of numerous biological, geological materials together with polymers and various food products. Later, Kosterin[3] disclosed that Reiner–Rivlin rheological relation is inappropriate in articulating the influences of normal stresses. The flow of Reiner–Rivlin fluid past rectangular ducts is analyzed numerically by Gao and Hartnett[4]. The interesting outcome of this study revealed that the heat transfer increases substantially in attendance of the second normal stresses. Attia[5] obtained a numerical solution of the unsteady flow of Reiner–Rivlin fluid past a rotating permeable disk with impacts of suction/injection. The major conclusion of this study is that the heat transfer effect is more significant in the presence of suction in comparison to the injection. In another study Attia[6] discussed the flow of the Reiner–Rivlin liquid with Ion slip and Hall current impacts past a rotating disk. An interesting result of this investigation points out that the effect of the Ion slip on the axial velocity is more obvious for Reiner–Rivlin fluid as compared to any Newtonian liquid. The numerical solution of the Reiner–Rivlin fluid flow with partial slip owing to a rotating disk is deliberated by Tabassum and Mustafa[7]. This research disclosed that higher values of the torque and slip parameter are needed to keep the steady rotation of the disk. The study of[7] is extended by Naqvi et al.[8] discussing the numerical solution of the Reiner–Rivlin liquid flow due to a rotating disk with multiple slips. A decline in the radially outward flow is perceived owing to an upsurge in the Reiner–Rivlin liquid parameter is a key outcome of this study. In a recent study, Rashid and Mustafa[9] discussed the heat transfer with entropy generation analysis of Von Karman flow owing to a rotating disk of the Reiner–Rivlin liquid. The salient result of this study is that in the case of the Reiner–Rivlin fluid the moment coefficient is significantly decreased.

The bacteria and the microalgae possess high density in comparison to the water and because of this fact they move in an upward direction opposite to gravity. Owing to this phenomenon the top layer becomes thicker than the bottom one and creates an unhinged situation as far as density distribution is concerned. Following the physics of the problem, convective patterns are formed because of the convective instability in this case.

Authors	Reiner–Rivlin flow model	Nanofluid flow over a rotating disk	Cattaneo–Christov flow heat flux	Impact of Bioconvection	Entropy generation analysis	Arrhenius activation energy, chemical reaction
Tabassum et al.[7]	Yes	No	No	No	No	No
Naqvi et al.[8]	Yes	Yes	No	No	No	No
Rashid et al.[9]	Yes	No	Yes	No	Yes	No
Present	**Yes**	**Yes**	**Yes**	**Yes**	**Yes**	**Yes**

Table 1. Literature survey for novelty of the envisioned model.

Such random instantaneous pattern activity of microorganisms is termed as the bioconvection. Bioconvection is categorized as geotactic[10, 11], gyrotactic[12, 13], and chemotactic[14]. Bioconvection applications may be found in numerous industrial, ecological, and commercial products including fertilizers, ethanol, ecological fuels, and fuel cells. Waqas et al.[15] studied numerically the flow of Oldroyd-B nanoliquid with motile microorganism impact past a rotating disk. The numerical solution of the transient flow of the rate type thin film nanofluid flow over a rotating disk with bioconvection, activation energy, and Ohmic heating is studied by Abdelmalek et al.[16]. It is inferred from this study that axial and tangential velocities are reduced when the buoyancy ratio parameter is boosted. Ramzan et al.[17] uncovered a numerical solution of the nanofluid flow containing carbon nanotubes with dust particles over an inclined rotating disk. It is witnessed in this exploration that the thermal field is stronger in the case of the nanofluid phase in comparison to the dust phase and this effect becomes stronger when the impact of the thermal radiation is augmented. Some recent explorations featuring flow over the rotating disk may be found in[18–21].

In a system and its surroundings, entropy tests the rate of disorder. It is a physical occurrence of heat transfer in the form of energy. Because of any friction or dislocation of particles, the movement of heat induces a difference in potential energy and kinetic energy etc. Bejan[22] was a initiator, who studied the entropy generation analysis during heat losing procedure of fluid motion. Ijaz et al.[23] deliberated the Sisko nanofluid with activation energy and entropy generation in non-linear radiative heat flux. It is noticed that entropy generation is increased for mounting values of the Brinkman number. Wakeel et al.[24] examined the Hall effects in second-grade fluid flow with C–C heat flux and entropy generation over a rotating stretchable disk. The flow of Marangoni Maxwell fluid past a rotating disk accompanying the thermal radiation and activation energy is examined numerically by Devi and Mabood[25]. The salient outcome highlighting the entropy generation impact is that the higher estimates of the Bejan number and the fluid parameter weaken the entropy generation rate. Abbas et al.[26] discussed the numerical solution of the MHD nanofluid flow over a rotating disk with second-order velocity slip and activation energy with entropy minimization optimization. The main finding of the envisioned model is that the entropy generation is influenced by the magnetic field. Some latest publications focusing on the impact of entropy may be found in[27–29].

It is a learned phenomenon that the transfer of heat arises due to temperature differences amongst two different objects or within a similar body. Fourier law (heat conduction) possesses a drawback that any disturbance instigated in the beginning will carry out throughout the process. To resolve this issue, Cattaneo introduced thermal relaxation time for Fourier's law (heat conduction) which allows the transport of heat by waves propagating with controlled speed[30]. Later, Christov developed the relation proposed by Cattaneo through frame-indifferent change with the Oldroyd upper-convected derivative. Such relation is entitled as C–C flux model. Shehzad et al.[31] studied MHD incompressible Maxwell bioconvection fluid flow over a rotating isolated disk in the presence of C–C heat flux. The flow of Oldroyd-B fluid with C–C heat flux over a rotating disk is studied by utilizing the BVP Midrich numerical technique. It is noticed in this exploration that the fluid velocity is affected by the thermal relaxation parameter. Hayat et al.[32] using Homotopy Analytic scheme found an analytical solution of the Newtonian fluid over a rotating disk having variable thickness with C–C heat flux. The key observation revealed that the surface drag coefficient is affected when the thickness of the disk is increased. Recent studies focusing on the impact of C–C heat flux may be found in[33–35].

The aforementioned studies disclosed that abundant researches are available in the literature discussing the flow of fluid over a rotating disk. Nevertheless, restricted literature may be found that deliberates the Reiner–Rivlin nanofluid flow over a rotating disk. But no study so far is not attempted that ponders the flow of Reiner–Rivlin nanofluid over a rotating disk with bioconvection, Arrhenius activation energy, C–C heat flux, and entropy generation analysis. The numerical result to the model is found. The abundant applications related to nanofluids may be found in the engineering and industrial processes including electronics applications, transportation, Nanofluids-based microbial fuel cell, industrial cooling applications, Energy storage, Heating buildings and reducing pollution, Space and defense, Magnetic sealing, Antibacterial activity, Nanodrug delivery, Intensify microreactors, Nuclear systems cooling, Mass transfer enhancement, Solar absorption, Mechanical applications, Friction reduction, Nanofluids as vehicular brake fluids, and nanofluids with unique optical properties. The inimitability of the current model as portrayed in Table 1 by associating the present model with the published studies.

Mathematical modeling

Consider a steady axial symmetric three-dimensional incompressible Reiner–Rivlin nanofluid flow rotating with the angular velocity ω with $z > 0$, over a rotating disk coinciding with the plane $z = 0$, (Fig. 1). Let u, v and w be the velocity components along the directions of growing r, φ and z respectively. Because of the axial symmetry, the velocity components are assumed to be independent of the azimuthal coordinate φ[7]. The slip and convective
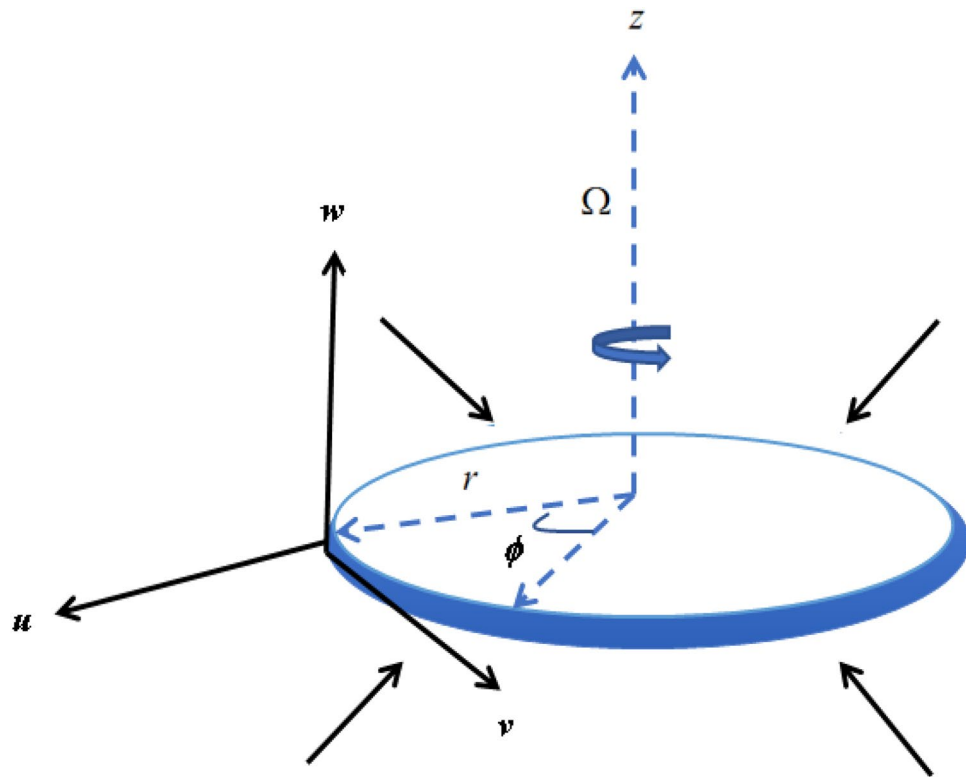
Figure 1. Flow geometry.

boundary conditions are applied. The impact of activation energy, gyrotactic microorganism, and C–C heat flux in a porous medium are also considered. Entropy generation is also a part of this model.

Following Reiner[1] and Rivlin[2], we have the following stress tensor for the flow field:

$$\tau_{ij} = -p\delta_{ij} + \mu e_{ij} + \mu_c e_{ik}e_{kj}; \quad e_{jj} = 0. \tag{1}$$

Here μ_c is the coefficient of cross-viscosity, δ_{ij} is the Kronecker delta, e_{ij} is the tensor of deformation rate and p is the pressure. The governing boundary layer equations under the impact of C–C heat flux are represented as:

$$u_r + \frac{u}{r} + w_z = 0 \tag{2}$$

$$\rho\left(uu_r + wu_z - \frac{v^2}{r}\right) = (\tau_{rr})_r + (\tau_{rz})_r + \frac{\tau_{rr} - \tau_{\varphi\varphi}}{r} - \frac{v}{k}u, \tag{3}$$

$$\rho\left(uv_r + wv_z + \frac{uv}{r}\right) = \frac{1}{r^2}\left((2r\tau_{r\varphi}) + r^2(\tau_{r\varphi})_r\right) + (\tau_{z\varphi})_z + \frac{\tau_{r\varphi} - \tau_{\varphi r}}{r} - \frac{v}{k}v, \tag{4}$$

$$\rho(uw_r + ww_z) = \frac{1}{r}(\tau_{rz} + r(\tau_{rz})_r) + \tau_{zz} - \frac{v}{k^*}w, \tag{5}$$

$$uT_r + wT_z = \alpha_m\left(T_{rr} + \frac{1}{r}T_r + T_{zz}\right) + \frac{(\rho c)_p}{(\rho c)_f}\left(\begin{array}{c}D_B(T_rC_r + T_zC_z)\\ +\frac{D_T}{T_\infty}((T_r)^2 + (T_z)^2)\end{array}\right)$$
$$- \lambda_2\left(u^2T_{rr} + w^2T_{zz} + 2uwT_{rz} + (uu_r + wu_z)T_r + (uw_r + ww_z)T_z\right) + q^*, \tag{6}$$

$$q^* = \frac{k_\infty U_w}{zv(\rho c)_f}\left\{A^*(T_w - T_\infty)f + B^*(T - T_\infty)\right\} \tag{7}$$

$$uC_r + wC_z = D_B\left(C_{rr} + \frac{1}{r}C_r + C_{zz}\right) + \frac{D_T}{T_\infty}\left(T_{rr} + \frac{1}{r}T_r + T_{zz}\right) - k_r^2(C - C_\infty)\left(\frac{T}{T_\infty}\right)^n e^{\left(\frac{-E_a}{kT}\right)}, \tag{8}$$

4

$$uN_r + wN_z + \frac{bW_c}{C_w - C_\infty}(N_zC_z + NC_z) = D_n\left(N_{rr} + \frac{1}{r}N_r + N_{zz}\right). \tag{9}$$

The associated boundary conditions are given as:

$$u(r,0) = \beta_1\tau_{rz}(r,0) \quad v(r,0) = \beta_2\tau_{z\varphi}(r,0) + r\Omega, \quad w(r,0) = 0,$$
$$-kT_z(r,0) = h_f(T_w - T(r,0)), \quad -D_BC_z = h_s(C_w - C(r,0)) \quad -D_nN_z = h_n(N_w - N(r,0)),$$
$$u \to 0, \quad v \to 0, \quad T \to T_\infty, \quad C \to C_\infty, \quad N \to N_\infty. \tag{10}$$

Components of deformation rate tensors[2] are:

$$e_{rr} = 2u_r, e_{\phi\phi} = 2\frac{u}{r}, e_{zz} = 2w_z, e_{r\phi} = e_{\phi r} = r\left(\frac{v}{r}\right)_r,$$
$$e_{z\phi} = e_{\phi z} = v_z, e_{rz} = e_{zr} = u_z + w_r, \tag{11}$$

and the components of the stress tensor is given by[7]:

$$\tau_{rr} = -p + \mu(2u_r) + \mu_c\left\{4(u_r)^2 + (u_z + w_r)^2 + \left(v_r - \frac{v}{r}\right)^2\right\}, \tag{12}$$

$$\tau_{zr} = \mu(u_z + w_r) + \mu_c\left\{(2u_r)(u_z + w_r) + v_z\left(v_r - \frac{v}{r}\right) + 2w_z(u_z + w_r)\right\} \tag{13}$$

$$\tau_{\phi\phi} = -p + \mu\left(2\frac{u}{r}\right) + \mu_c\left\{\left(4\frac{u^2}{r^2}\right)(v_z)^2 + \left(v_r - \frac{v}{r}\right)^2\right\}, \tag{14}$$

$$\tau_{r\phi} = \mu\left(v_r - \frac{v}{r}\right) + \mu_c\left\{(2u_r)\left(v_r - \frac{v}{r}\right) + \left(2\frac{u}{r}\right)\left(v_r - \frac{v}{r}\right) + 2v_z(u_z + w_r)\right\}, \tag{15}$$

$$\tau_{z\phi} = \mu(v_z) + \mu_c\left\{(u_z + w_r)\left(v_r - \frac{v}{r}\right) + 2\left(\left(\frac{u}{r}\right)(v_z) + w_z(v_z)\right)\right\}. \tag{16}$$

Transformations are:

$$\eta = \sqrt{\frac{\Omega}{\nu}}z, \quad u = r\Omega f'(\eta), \quad v = r\Omega g(\eta), \quad w = -2\sqrt{\Omega\nu}f(\eta),$$
$$\theta = \frac{T - T_\infty}{T_w - T_\infty}, \quad \xi = \frac{N - N_\infty}{N_w - N_\infty}, \quad \varphi = \frac{C - C_\infty}{C_w - C_\infty}, \tag{17}$$

Using Eq. (17), Eqs. (3), (4), and (6)–(9) become:

$$f''' - f'^2 + 2ff'' + g^2 - \lambda f' + K(f''^2 - g'^2 - 2f'f'') = 0 \tag{18}$$

$$g'' - 2f'g + 2fg' - \lambda g - 2K(f'g'' - f''g') = 0, \tag{19}$$

$$\theta'' + \Pr f'\theta + N_b\theta'\phi' + N_t\theta'^2$$
$$- \gamma \Pr(ff''\theta' + f^2\theta'') + Af' + B\theta + N_b\theta'\phi' + N_t\theta'^2 = 0, \tag{20}$$

$$\phi'' + 2Scf\phi' + \frac{N_b}{N_t}\theta'' - K_1\phi(1 + \delta\theta)^n e^{\frac{-E}{1+\delta\theta}} = 0, \tag{21}$$

$$\xi'' - Pe\left(\xi'\phi' + (\xi + \Omega_1)\phi''\right) + 2Lbf\xi' = 0. \tag{22}$$

$$f'(0) = \alpha_1 f''(0)\left[1 - 2Kf'(0)\right], \quad f(0) = 0, \quad g(0) = \alpha_2 g'(0)\left[1 - 2Kf'(0)\right] + 1, \quad \theta'(0) = -B_1(1 - \theta),$$
$$\phi' = -B_2(1 - \phi), \quad \xi' = -B_3(1 - \xi),$$
$$f'(\infty) = 0, \quad g(\infty) = 0, \theta(\infty) = 0, \quad \phi(\infty) = 0, \quad \xi(\infty) = 0, \tag{23}$$

The quantities in the above equations are defined as:

$$\lambda = \frac{v}{k\Omega}, \quad \gamma = \lambda_1 \Omega, \quad N_b = \frac{\tau D_B (C_w - C_\infty)}{v}, \quad N_t = \frac{\tau D_T \Delta T}{T_\infty v}, \quad \alpha_2 = \rho \sqrt{\Omega v} \beta_2, \quad B_3 = \frac{h_n}{D_n} \sqrt{\frac{v}{\Omega}},$$

$$K = \frac{\mu_c \Omega}{\mu}, \quad B_1 = \frac{h_f}{k} \sqrt{\frac{v}{\Omega}}, \quad E = \frac{E_a}{kT_\infty}, \quad K_1 = \frac{k_r^2}{\Omega}, \quad \alpha_1 = \rho \sqrt{\Omega v} \beta_1, \quad B_2 = \frac{h_s}{D_B} \sqrt{\frac{v}{\Omega}}, \qquad (24)$$

$$Pe = \frac{bW_c}{D_m}, \quad \delta = \frac{\Delta T}{T_\infty}, \quad Lb = \frac{v}{D_m}, \quad \Omega = \frac{N_\infty}{N_f - N_\infty}, \quad Pr = \frac{\mu c_p}{k}, \quad Sc = \frac{v}{D_B}.$$

Drag force coefficient, the rates of heat, mass, and the local motile microorganisms' flux are defined by:

$$C_f = \frac{\sqrt{\tau_r^2 - \tau_\varphi^2}}{\rho u_w^2}, \quad Sh_x = \frac{rj_w}{D_n(C_w - C_\infty)}, \quad Nu_x = \frac{xq_n}{D_m(N_w - N_\infty)}. \qquad (25)$$

The dimensionless Skin friction coefficient, rate of heat, and mass fluxes and are the local motile microorganisms' flux are given as:

$$C_f \sqrt{\mathrm{Re}_x} = \sqrt{[f''(0))^2 - (g'(0)]^2}, \quad Sh\sqrt{\mathrm{Re}_x} = -\phi'(0).$$

$$Nu_x \sqrt{\mathrm{Re}_x} = -\xi'(0) \qquad (26)$$

Entropy generation analysis.

Following the volumetric entropy generation is presented in[22]:

$$S_G = \frac{k}{T_\infty^2}(T_z)^2 + \frac{1}{T_\infty} \left(\begin{array}{c} 2u_r \tau_{rr} + 2\left(\frac{1}{r}v_\phi + \frac{u}{r}\right)\tau_{\phi\phi} + 2w_z \tau_{zz} + 2\left(\frac{1}{r}u_\phi + \left(\frac{v}{r}\right)_r\right)\tau_{\phi r} \\ + w_r \tau_{rz} + \frac{1}{r}w_\phi \tau_{z\phi} \end{array} \right)$$

$$+ \frac{R_D}{T_\infty} T_z C_z + \frac{R_D}{C_\infty}(C_z)^2 + \frac{R_D}{n_\infty}(N_z)^2 + \frac{R_D}{T_\infty} N_z C_z + \frac{\mu u^2}{T_\infty k}. \qquad (27)$$

The entropy generation in the dimensionless form can be derived as:

$$N_G = \frac{S_G}{S_0'''} = \Omega_1 \theta'^2 + Br\left(\left[\frac{1}{\mathrm{Re}}f'^2 + \lambda f'^2 + \frac{16}{\mathrm{Re}}Kf'^3 - 2Kf'^3 - 2Kf'f''^2 - 2Kf'g'^2\right]\right)$$

$$+ L\theta'\phi' + L\frac{\Omega_2}{\Omega_1}\phi'^2 + L_1 \xi'\theta' + L_1\frac{\Omega_3}{\Omega_1}\xi'^2. \qquad (28)$$

where

$$Br = \frac{\mu\Omega^2}{k(T_0 - T_\infty)}, \quad \sigma_1 = \frac{(T_0 - T_\infty)}{T_\infty}, \quad L = \frac{R_D(C_w - C_\infty)}{k}, \quad L_1 = \frac{R_D(N_w - N_\infty)}{k},$$

$$\sigma_2 = \frac{(C_w - C_\infty)}{C_\infty}, \quad \sigma_3 = \frac{(N_w - N_\infty)}{N_\infty}, \quad S_0''' = \frac{k(T_0 - T_\infty)}{vT_\infty}. \qquad (29)$$

Graphical and tabulated outcomes with discussion

This sector (Figs. 2, 3, 4, 5, 6, 7, 8, 9, 10, 11, 12, 13, 14, 15, 16, 17, 18, 19, 20, 21) is dedicated to examining the influence of varied evolving parameters on the flow model involved profiles. The ranges of the parameters are defined as:

$$0.0 \le K \le 0.7, 0.5 \le \alpha_1, \alpha_2 \le 2.0, 0.1 \le \lambda \le 0.7, 0.4 \le B_1 \le 0.7, 0.5 \le \gamma \le 2.0, -0.9 \le A \le 0.9, -0.4 \le B \le 0.4,$$

$$0.1 \le \delta \le 1.3, 0.0 \le n \le 3.0, 0.1 \le E \le 0.7, 0.4 \le Lb \le 0.7, 1.0 \le Br \le 5.0, 0.5 \le \Omega_2 \le 0.8, 0.5 \le \mathrm{Re} \le 3.0.$$

The behavior of Reiner–Rivlin fluid parameter K on the axial, radial, and tangential velocities, and temperature profile is revealed in Figs. 2, 3, 4 and 5 for the uniform wall roughness. It is noticed from Figs. 2 and 3 that the axial and radial velocities are dwindled near the disk and augmented when striding far afield from it. As the fluid move in the direction of the axis of rotation, the centrifugal forces along with viscoelastic effects generates a wake flow in the radial direction and a lesser amount of liquid is seen along an axial path. That is why the axial velocity profile attains its maximum near the disk and diminishes away from the disk. However, contrary to axial and radial profiles, the azimuthal velocity profile attains an opposite trend (Fig. 4). Similarly, in Fig. 5 the fluid temperature is enhanced for growing estimates of K. Here, the thermal boundary layer thickness expands when the comparatively cold water is taken along the axial direction. Figures 6 and 7 represent the outcomes of the wall slip parameters α_1, α_2 versus the radial and tangential velocity components when K = 1. Here, it is further assumed that estimates of both α_1, α_2 are equal. It is noticed that the radial velocity is more away from the disk for large values of α_1, α_2 and an opposing trend is seen near it. The azimuthal velocity component possesses a reverse impact for the estimates of α_1, α_2. This is because of the disk's rotational impact that is partly transferred to the adjacent boundary layer. The impact of the permeability parameter λ versus radial and azimuthal distributions is shown in Figs. 8 and 9. It is noticed that both velocity profiles dwindle for large values of λ. Physically,
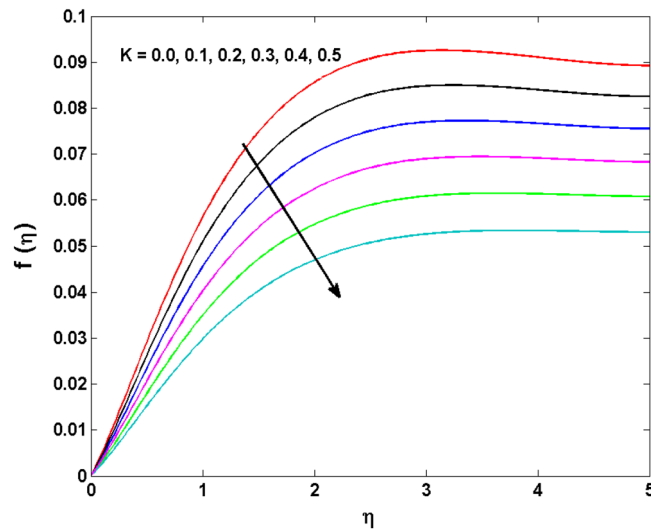
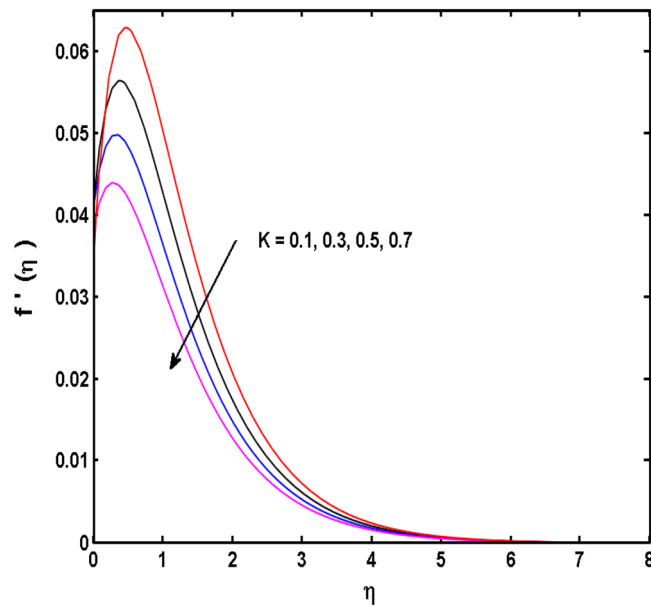**Figure 2.** Variations of K to $f(\eta)$.

Figure 3. Variations of K to $f'(\eta)$.

the movement of the liquid is hindered due to the occurrence of permeable media, and as a result, a falloff in the fluid velocities is seen.

The behavior of the conjugate parameter B_1 on temperature distribution is studied in Fig. 10. It is noticed that temperature and thermal boundary layer thickness are boosted for large estimates of B_1. Here, the increment in B_1 instigating the heat transfer that pushes extra heat from the surface. In this way, the temperature is enhanced. Figure 11 is illustrated to show the influence of the thermal relaxation parameter γ on the temperature profile. It is noted that the fluid temperature is decreased for large values of the γ. Large values of the γ points out the strong characteristics of the insulating material which are responsible for the drop in the fluid temperature. The influence of A and B (heat source and sink) on the temperature distribution is analyzed in Figs. 12 and 13. It is perceived that the temperature profile is rising when the values of both A, B are increased. Since the occurrence of heat source parameter produces more heat within the nanofluid flow field which leads to an increment in the boundary layer thickness. Hence, more heat in the nanofluid enhances the fluid temperature. Figures 14 and 15 are drawn to witness the impact of temperature difference parameters δ and n on the concentration distribution profile. It is witnessed that concentration distribution is a diminishing function for both δ and n. This shows that the concentration boundary layer thickness growing when the difference between ambient and wall temperatures is increased. The influence of the chemical reaction parameter K_1 and the activation energy parameter E against
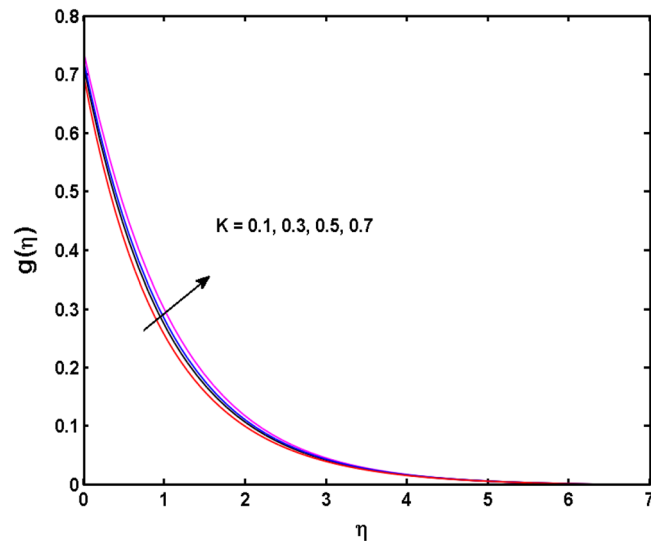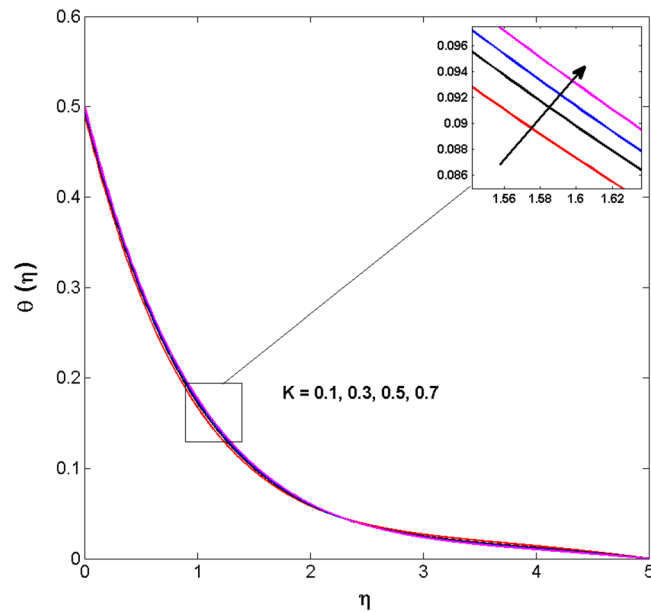
Figure 4. Variations of K to $g\,(\eta)$.

Figure 5. Variations of K to $\theta\,(\eta)$.

the concentration profile is portrayed in Fig. 16. It is seen that the concentration of the fluid weakens once the estimates of K_1 are augmented. Large values of K_1 are associated with the destructive chemical reaction and this eventually dissolves the fluid species. That is why the liquid concentration is reduced and an opposite behavior is noticed for E. Here, the generative case is strengthened for large estimates of E. As a result concentration is enhanced. The variation of bioconvection Lewis number Lb, and Peclet number Pe, on the fluid motile density is revealed in Fig. 17. It is detected that the motile density profile decreases for large values of the Peclet number. For the higher Pe, fluid motile density is decreased due to the decline in the diffusivity of microorganisms. It is also observed for mounting estimations of Lb, causes falloffs of microorganisms hence the profile of motile density also drops in this case.

Figures 18, 19, 20 and 21 display the vital role of volumetric entropy generation for varied estimations of Br, Ω_2, Re and K. For greater Br, Ω_2 and Re entropy generation is increases. For large values of Br viscous dissipation generates less transfer rate and thus augments entropy generation rises. For $Br = 0$, viscous dissipative irreversibility disappears and only heat transfer irreversibility produce. The effect of Re on entropy generation is expressed in Fig. 20. For large estimates of the Reynolds number, the substantial motion of the fluid molecules is witnessed. Thus, escalating the entropy generation rate. Figure 21 reveals that for higher values of the Reiner–Rivlin parameter K entropy generation is declined.
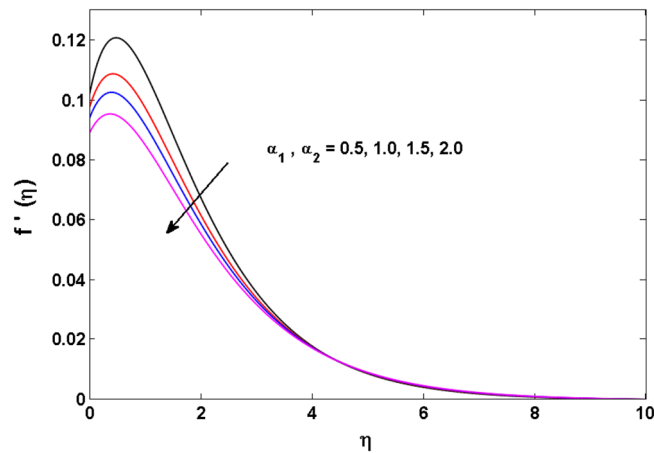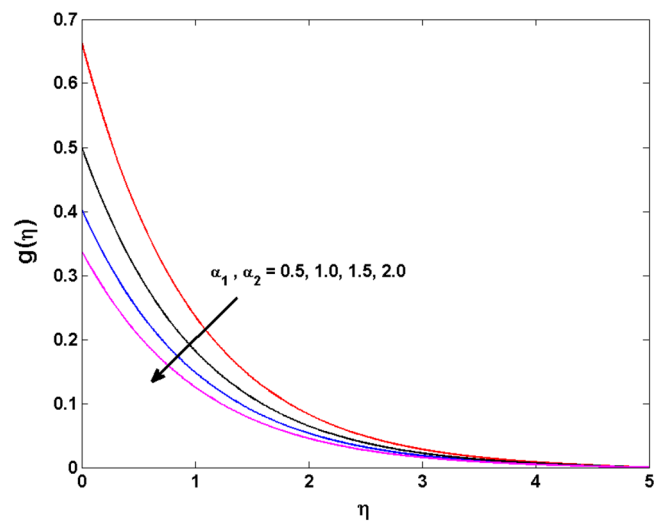
Figure 6. Variations of $\alpha_1,\ \alpha_2$ to $f'(\eta)$.

Figure 7. Variations of $\alpha_1,\ \alpha_2$ to $g(\eta)$.

Table 2 represents the numerical outcomes for skin friction coefficient, azimuthal velocity, entrainment velocity, and radial velocity for varied estimates of the slip and the Reiner–Rivlin parameters. Here, $f(\infty)$ helps in finding the volumetric flow rate of the von-Karman problem. The driving torque or the disk's torque is gauged through $g'(0)$. The viscoelastic impacts affect the torque in the Von Karman flow. The surface drag force coefficient and the resisting torque are enhanced for growing values of the radial and the tangential velocity components. It is comprehended that high torque at the disk shaft is enhanced for elevated values of the tangential slip parameter. It is also inferred from the tabulated values that skin friction coefficient and driving torque possess an increasing tendency for the Reiner–Rivlin parameter. However, an opposing trend is seen in the case of the volumetric flow rate. Table 3 portrays different variations of the rate of mass flux for different values of K, N_t, N_b, Pr and Sc. It is seen that for the large values of K, N_b and Pr Sherwood number decreases and the opposing effects are seen for N_t and Sc. Table 4 portrays different estimations in local density profile for various values of B_1, K, Pe and Lb. It is observed that for large estimates of B_1, Lb and Pe the local density number of microorganisms increases while falls off for greater parameter. Table 5 computes the numerical values of $f(\infty)$ for the increasing wall roughness parameter and Reiner–Rivlin parameter. The results obtained by using bvp4c are compared with Naqvi et al.[8]. An excellent harmony among both results is achieved.

Final remarks

In this study, the flow of the Reiner–Rivlin nanofluid generated by a rotating disk in the presence C–C heat flux and the gyrotactic microorganisms is deliberated. The flow is also accompanied by the effects of the heat source/sink, chemical reaction with activation energy with slip, and convective boundary conditions. The problem is solved numerically. The noteworthy observations of the model are appended as below:
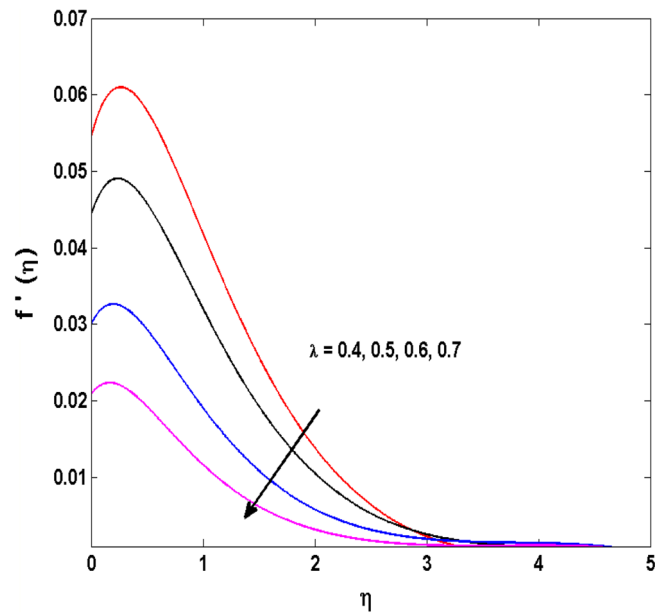
Figure 8. Variations of λ to $f'(\eta)$.
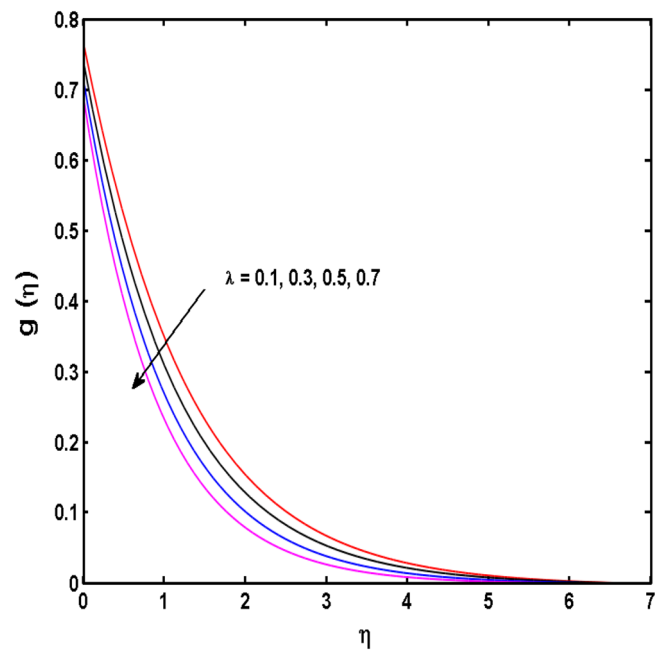

Figure 9. Variations of λ to $g(\eta)$.

- The radial and axial velocity components are diminishing functions for the Reiner–Rivlin parameter. However, an adverse impact is witnessed in the case of azimuthal velocity, and temperature profile.
- A diminishing impact of the slip parameters is perceived for both the radial and azimuthal velocity components.
- The permeability parameter shows dwindling influence versus the radial and tangential velocity components.
- Higher estimations of the thermal relaxation parameter cause reduction in the temperature profile.
- The fluid temperature is escalated for mounting estimates of the non-uniform heat source/sink parameter.
- The chemical reaction and the activation energy parameters possess an opposing impact on the concentration profile.
- The motile density profile diminishes for large values of the Peclet and the bioconvective Lewis numbers.
- The Brinkman and Reynolds numbers show opposing trends versus volumetric entropy generation.
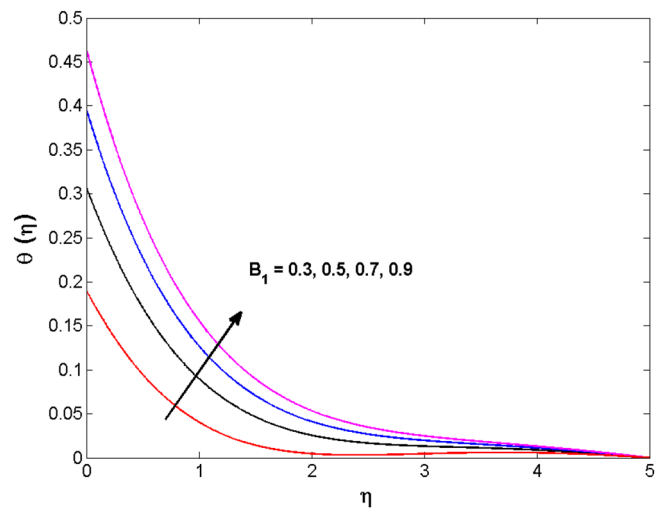
Figure 10. Variations of B_1 to $\theta(\eta)$.
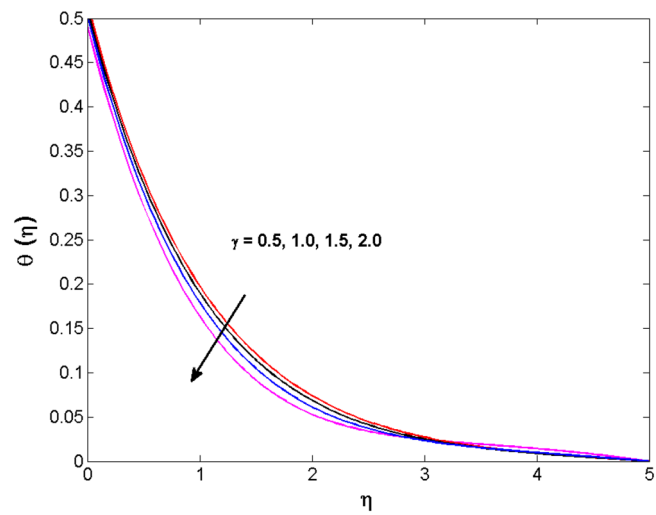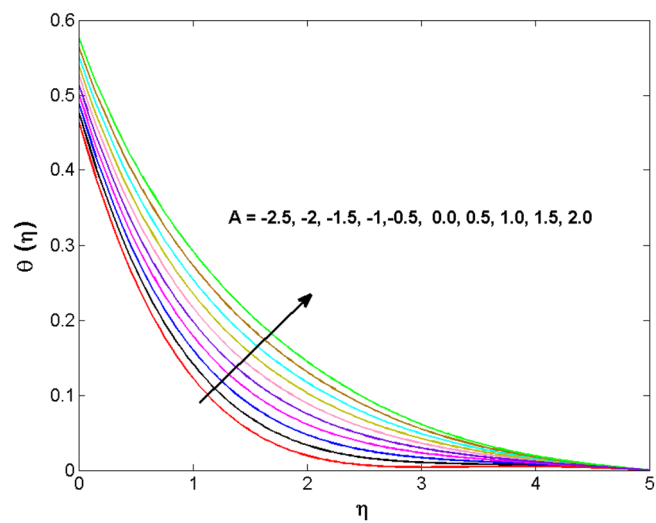

Figure 11. Variations of γ to $\theta(\eta)$.
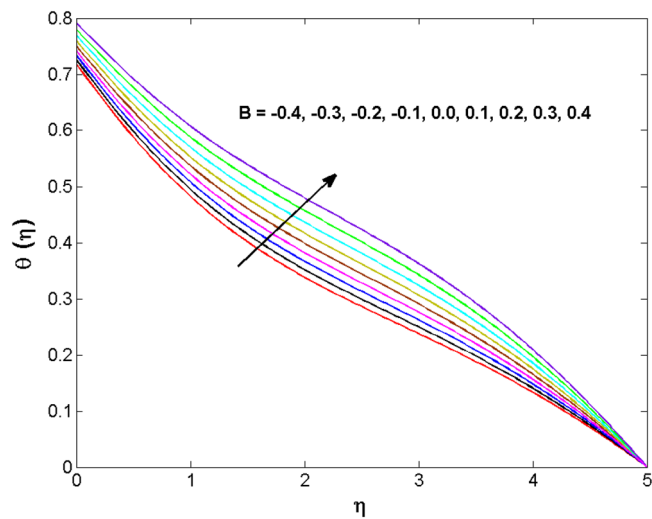

Figure 12. Variations of A to $\theta(\eta)$.
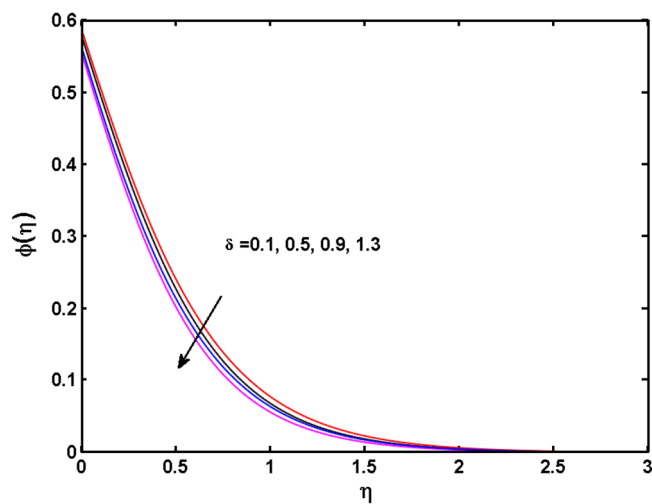
Figure 13. Variations of B to θ (η).

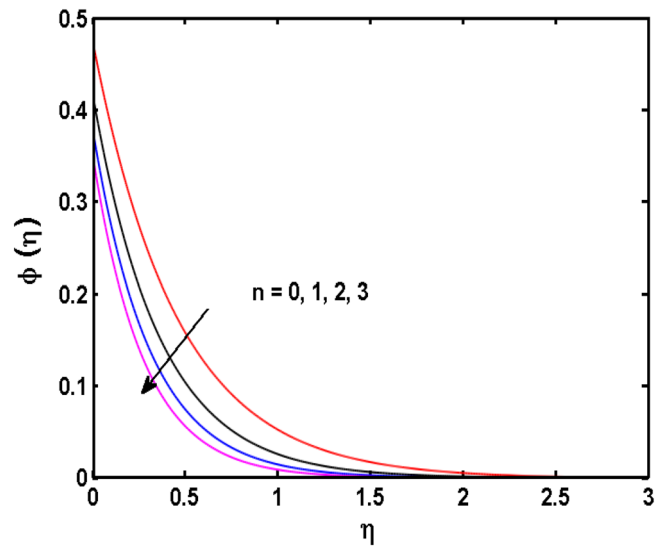**Figure 14.** Variations of δ to ϕ (η).

Figure 15. Variations of n to $\phi\ (\eta)$.
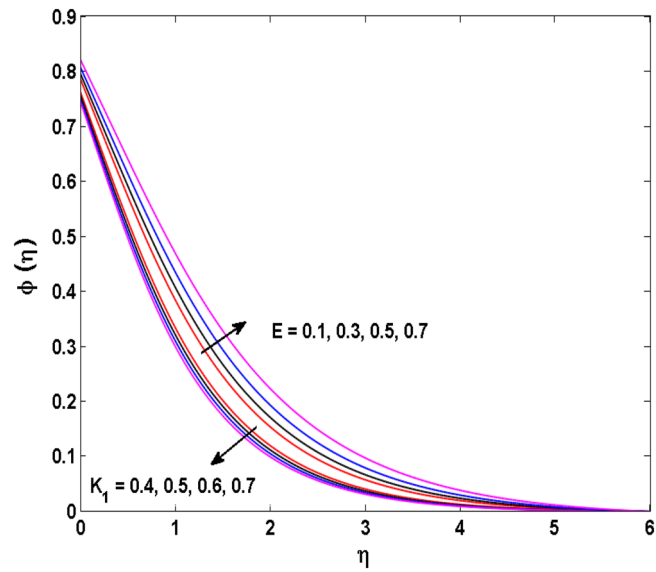
Figure 16. Variations of K_1 and E to $\phi\ (\eta)$.
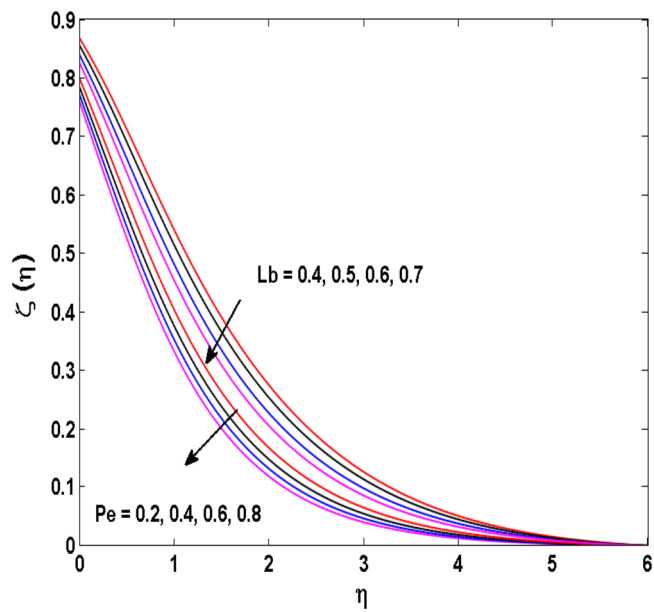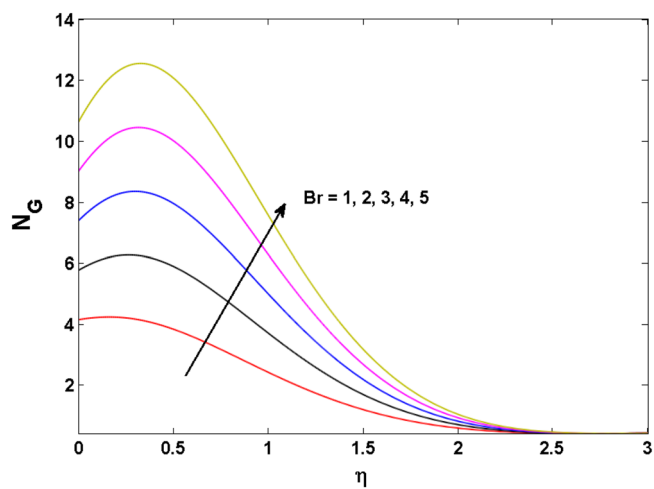
Figure 17. Variations of *Pe* and *Lb* to $\zeta\ (\eta)$.
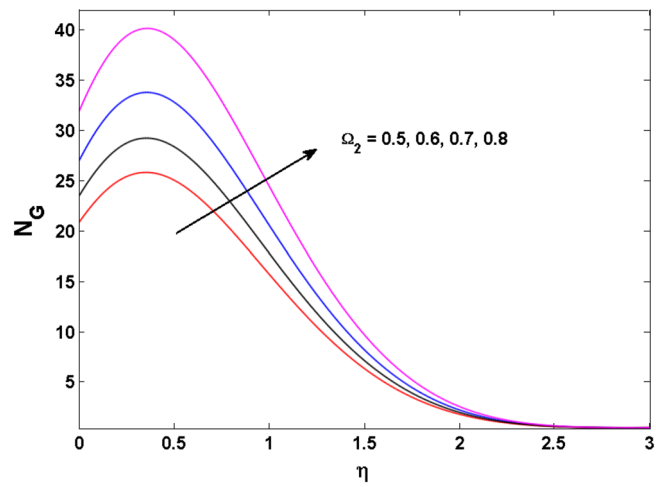

Figure 18. Variations of *Br* to N_G.

Figure 19. Variations of Ω_2 to N_G.
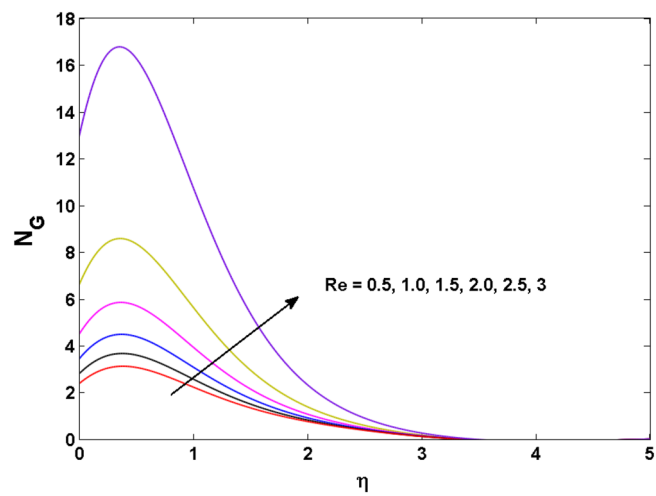
Figure 20. Variations of Re to N_G.
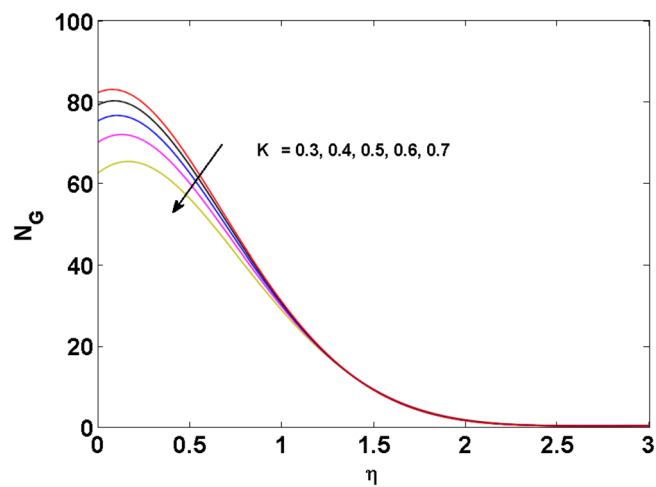
Figure 21. Variations of K to N_G.

α_1	α_2	K	$\sqrt{(f''(0))^2 + (g'(0))^2}$	$g'(0)$	$f(\infty)$	$f''(0)$
1	2	0.2	0.3101282	−0.30858225	0.058277735	0.030927356
1.5	2		0.3111269	−0.31012459	0.063644215	0.024953560
2	2		0.3749075	−0.31115555	0.067213467	0.020913603
2	2		0.3749075	−0.31115555	0.067213467	0.020913603
2	3		0.2353182	−0.23494064	0.044550026	0.013326333
2	4		0.1895022	−0.18927773	0.031514276	0.009220524
2	2	0.3	0.3126156	−0.31199346	0.063018309	0.019713295
		0.7	0.3131332	−0.31279718	0.045216515	0.014503586
		1	0.3139463	−0.31364883	0.031017367	0.010366372

Table 2. The tabulation of numerical results for Drag force $C_F \mathrm{Re}_x^{1/2}$ against the various values of α_1, α_2, K, parameters.

K	N_t	N_b	Pr	Sc	$-\varphi'(0)$
0.2	0.1	0.6	3	4	0.37790968
0.7					0.36797258
1					0.36235873
	0.3				0.42296784
	0.4				0.44798048
	0.5				0.47456857
		0.15			0.42183083
		0.2			0.40723295
		0.3			0.39261496
			4		0.3945757
			6		0.38030306
			8		0.36270411
				1	0.3945757
				3	0.49663337
				5	0.55345741
					0.39615661
					0.3945757
					0.39407366

Table 3. Numerical results for $Sh_x \mathrm{Re}^{-0.5}$ against the various values of the K, N_t, N_b, Pr, Sc, and β parameters.

B_1	K	Pe	Lb	$-\xi'(0)$
0.2	0.2	0.2	1	0.17235092
0.3				0.23692559
0.4				0.29148902
	0.2			0.42313856
	0.7			0.39628911
	1			0.37841022
		0.3		0.34334759
		0.4		0.36772149
		0.5		0.39067931
			1.5	0.32953031
			2	0.34081314
			2.5	0.35143172

Table 4. The tabulation of numerical results for $Nu_x \mathrm{Re}^{-0.5}$ against the various values of the K, Pe, and Lb parameters.

α_1	α_2	K	Naqvi et al.[8] $f(\infty)$	Present results bvp4c $f(\infty)$
1	2	1	0.289891	0.289893
1.5	2	1	0.298954	0.298958
2	2	1	0.305295	0.305298
2	2	1	0.305295	0.305299
2	3	1	0.277820	0.277860
2	4	1	0.256126	0.256130
2	2	0.2	0.372886	0.372889
2	2	0.7	0.317290	0.317299
2	2	0.9	0.052950	0.053000

Table 5. The tabulation of numerical results of $f(\infty)$ by keeping $\mathrm{Pr} = 7, Sc = 0.5, \ N_t = 0.1, N_b = 0.6.$

References

1. Reiner, M. A mathematical theory of dilatancy. *Am. J. Math.* **67**(3), 350–362 (1945).
2. Rivlin, R. S. The hydrodynamics of non-Newtonian fluids. I. *Proc. R. Soc. Lond. Ser. A Math. Phys. Sci.* **193**(1033), 260–281 (1948).
3. Kosterin, A. F. Some rheological properties of Reiner–Rivlin fluids. *J. Eng. Phys.* **35**(3), 1121–1122 (1978).
4. Gao, S. X. & Hartnett, J. P. Heat transfer behavior of Reiner–Rivlin fluids in rectangular ducts. *Int. Commun. Heat Mass Transf.* **39**(6), 1317–1324 (1996).
5. Attia, H. A. Numerical study of the flow and heat transfer in a Renier–Rivlin fluid on a rotating porous disk. *J. Appl. Mech. Tech.* **46**(1), 68–76 (2005).
6. Attia, H. A. The effect of ion slip on the flow of Reiner–Rivlin fluid due a rotating disk with heat transfer. *J. Appl. Mech. Tech.* **21**(1), 174–183 (2007).
7. Tabassum, M. & Mustafa, M. A numerical treatment for partial slip flow and heat transfer of non-Newtonian Reiner–Rivlin fluid due to rotating disk. *Int. Commun. Heat Mass Transf.* **123**, 979–987 (2018).
8. Naqvi, S. M. R. S., Kim, H. M., Muhammad, T., Mallawi, F. & Ullah, M. Z. Numerical study for slip flow of Reiner–Rivlin nanofluid due to a rotating disk. *Int. Commun. Heat Mass Transf.* **116**, 104643 (2020).
9. Rashid, M. U. & Mustafa, M. A study of heat transfer and entropy generation in von Kármán flow of Reiner–Rivlin fluid due to a stretchable disk. *Ain Shams Eng. J.* https://doi.org/10.1016/j.asej.2020.06.017 (2020).
10. Winet, H. & Jahn, T. L. Geotaxis in Protozoa I. A propulsion—Gravity model for tetrahymena (Ciliata). *J. Theor. Biol.* **46**(2), 449–465 (1974).
11. Kuznetsov, A. V. & Jiang, N. Bioconvection of negatively geotactic microorganisms in a porous medium: the effect of cell deposition and declogging. *Int. J. Numer. Methods Heat Fluid Flow* **13**(3), 341–364 (2003).
12. Ghorai, S. & Hill, N. A. Wavelengths of gyrotactic plumes in bioconvection. *Bull. Math. Biol.* **62**(3), 429–450 (2000).
13. Sharma, Y. D. & Kumar, V. The effect of high-frequency vertical vibration in a suspension of gyrotactic micro-organisms. *Mech. Res. Commun.* **44**, 40–46 (2012).
14. Yanaoka, H., Inamura, T. & Suzuki, K. Numerical analysis of bioconvection generated by chemotactic bacteria. *J. Fluid Sci.* **4**(3), 536–545 (2009).
15. Waqas, H., Imran, M., Muhammad, T., Sait, S. M. & Ellahi, R. Numerical investigation on bioconvection flow of Oldroyd-B nanofluid with nonlinear thermal radiation and motile microorganisms over rotating disk. *J. Therm. Anal. Calorim.* https://doi.org/10.1007/s10973-020-09728-2 (2020).
16. Abdelmalek, Z., Khan, S. U., Waqas, H., Al-Khaled, K. & Tlili, I. A proposed unsteady bioconvection model for transient thin film flow of rate-type nanoparticles configured by rotating disk. *J. Therm. Anal. Calorim.* https://doi.org/10.1007/s10973-020-09698-5 (2020).
17. Ramzan, M. *et al.* Numerical simulation of 3D condensation nanofluid film flow with Carbon nanotubes on an inclined rotating disk. *Appl. Sci.* **10**(1), 168 (2020).
18. Ramzan, M., Chung, J. D. & Ullah, N. Partial slip effect in the flow of MHD Micropolar nanofluid flow due to a rotating disk—A numerical approach. *Results Phys.* **7**, 3557–3566 (2017).
19. Zhou, S. S. *et al.* 3D Bio-convective nanofluid slip flow comprising gyrotactic microorganisms over a stretched stationary disk with modified Fourier law. *Phys. Scr.* **96**(7), 075702 (2021).
20. Ramzan, M. *et al.* Upshot of heterogeneous catalysis in a nanofluid flow over a rotating disk with slip effects and Entropy optimization analysis. *Sci. Rep.* **11**(1), 1–15 (2021).
21. Mehmood, T., Ramzan, M., Howari, F., Kadry, S. & Chu, Y. M. Application of response surface methodology on the nanofluid flow over a rotating disk with autocatalytic chemical reaction and entropy generation optimization. *Sci. Rep.* **11**(1), 1–18 (2021).
22. Bejan, A. & Kestin, J. Entropy generation through heat and fluid flow. *J. Appl. Mech.* **50**, 475 (1983).
23. Ijaz, M., Ayub, M. & Khan, H. Entropy generation and activation energy mechanism in nonlinear radiative flow of Sisko nanofluid: rotating disk. *Heliyon* **5**(6), e01863 (2019).
24. Wakeel Ahmad, M., McCash, L. B., Shah, Z. & Nawaz, R. Cattaneo–Christov heat flux model for second grade nanofluid flow with Hall effect through Entropy generation over stretchable rotating disk. *Coatings* **10**(7), 610 (2020).
25. Devi, S. S. U. & Mabood, F. Entropy anatomization on Marangoni Maxwell fluid over a rotating disk with nonlinear radiative flux and Arrhenius activation energy. *Int. Commun. Heat Mass Transf.* **118**, 104857 (2020).
26. Abbas, S. Z. *et al.* Fully developed entropy optimized second order velocity slip MHD nanofluid flow with activation energy. *Comput. Methods Programs Biomed.* **190**, 105362 (2020).
27. Khan, M. W. A., Shah, F., Khan, M. I., Chu, Y. M. & Kadry, S. Fully developed entropy-optimized MHD nanofluid flow by a variably thickened rotating surface. *Appl. Phys.* **126**(11), 1–15 (2020).
28. Nayak, M. K., Patra, A., Shaw, S. & Misra, A. Entropy optimized Darcy–Forchheimer slip flow of $Fe_3 O_4 - CH_2 OH_2$ nanofluid past a stretching/shrinking rotating disk. *Heat Transf.* https://doi.org/10.1002/htj.21987 (2020).
29. Renuka, A., Muthtamilselvan, M., Doh, D. H. & Cho, G. R. Entropy analysis and nanofluid past a double stretchable spinning disk using homotopy analysis method. *Math. Compt. Simul.* **171**, 152–169 (2020).

30. Hafeez, A., Khan, M. & Ahmed, J. Thermal aspects of chemically reactive Oldroyd-B fluid flow over a rotating disk with Cattaneo–Christov heat flux theory. *J. Therm. Anal. Calorim.* **144**, 1–11 (2020).
31. Hayat, T., Kiran, A., Imtiaz, M. & Alsaedi, A. Cattaneo–Christov heat flux in flow by rotating disk with variable thickness. *Eur. Phys. J. Plus* **132**(3), 1–18 (2017).
32. Abid, N., Ramzan, M., Chung, J. D., Kadry, S. & Chu, Y. M. Comparative analysis of magnetized partially ionized copper, copper oxide–water and kerosene oil nanofluid flow with Cattaneo–Christov heat flux. *Sci. Rep.* **10**(1), 1–14 (2020).
33. Ramzan, M., Gul, H., Kadry, S. & Chu, Y. M. Role of bioconvection in a three dimensional tangent hyperbolic partially ionized magnetized nanofluid flow with Cattaneo–Christov heat flux and activation energy. *Int. Commun. Heat Mass Transf.* **120**, 104994 (2020).
34. Ramzan, M., Abid, N., Lu, D. & Tlili, I. Impact of melting heat transfer in the time-dependent squeezing nanofluid flow containing carbon nanotubes in a Darcy–Forchheimer porous media with Cattaneo–Christov heat flux. *Commun. Theor. Phys.* **72**(8), 085801 (2020).
35. Alebraheem, J. & Ramzan, M. Flow of nanofluid with Cattaneo–Christov heat flux model. *Appl. Nanosci.* **10**, 1–11 (2019).

Author contributions

M.R. supervised and conceived the idea; H.G. wrote the manuscript; Y.P.L. helped in writing—review, and editing of the revised version; J.D.C. worked on the software and funding acquisition; M.B. validate the revised results.

Funding

Competing interests

The authors declare no competing interests.

Additional information

Correspondence and requests for materials should be addressed to M.R.

Reprints and permissions information is available at www.nature.com/reprints.

Publisher's note Springer Nature remains neutral with regard to jurisdictional claims in published maps and institutional affiliations.